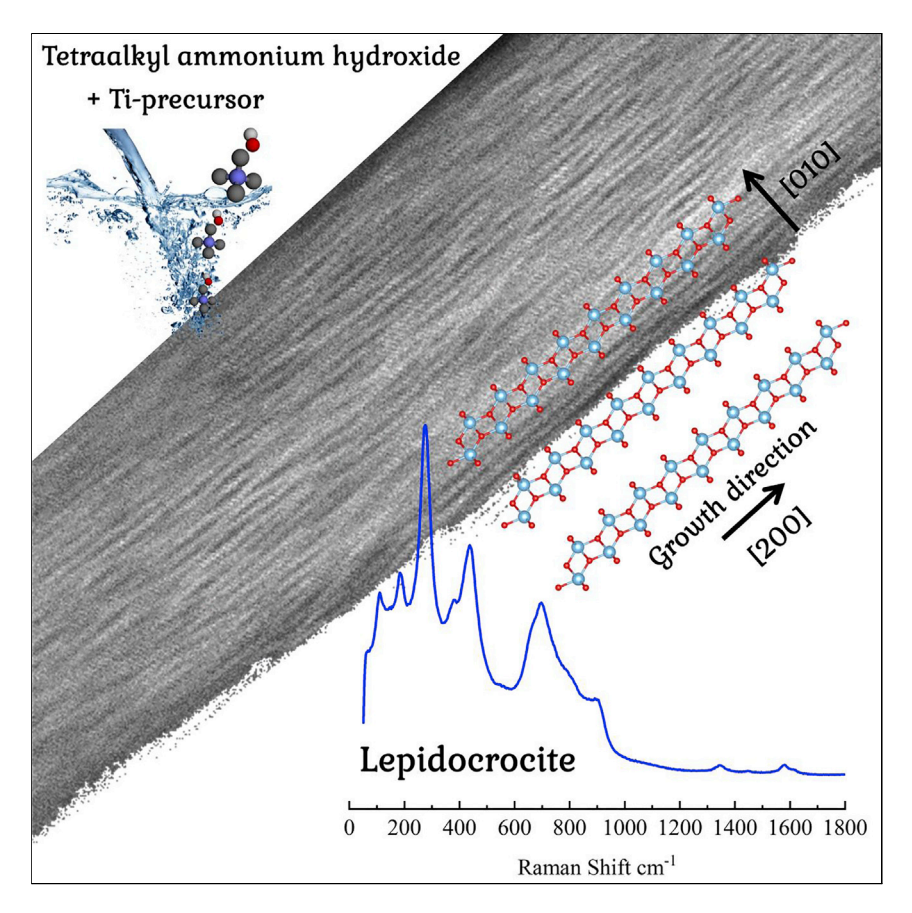
Matter



Article

On the structure of one-dimensional TiO₂ lepidocrocite



Recently, we discovered a one pot, cheap, scalable method to convert a dozen Ticontaining earth-abundant, non-toxic precursors (e.g., TiC, TiN) into TiO2-based one dimensional (1D) nanofilaments, (NFs). Using high-resolution STEM images, Raman, and XRD, we conclude the NFs have a TiO2 lepidocrocite structure. With some NF cross sections $\approx 5\times5\,\text{Å}^2$, the specific theoretical surface areas of >1000 m²/g are anticipated. The latter can partially explain the remarkable properties these materials already exhibit in photocatalysis, dye degradation, batteries, and supercapacitors.

Hussein O. Badr, Francisco Lagunas, Daniel E. Autrey, ..., Robert F. Klie, Yong-Jie Hu, Michel W. Barsoum

yh593@drexel.edu (Y.-J.H.) barsoumw@drexel.edu (M.W.B.)

Highlights

Scalable, cheap, one pot facile synthesis of titanium dioxide nanofilaments (NFs)

Raman HRTEM and XRD indicated the NF's structure is 1D TiO₂, lepidocrocite-based

TEM images suggest the smallest NFs may have cross sections of the order of $5 \times 5 \text{ Å}^2$

NFs grow along [100] and selfalign in two directions, viz. in- and out-of-plane



Badr et al., Matter 6, 128–141 January 4, 2023 © 2022 Elsevier Inc. https://doi.org/10.1016/j.matt.2022.10.015







Article

On the structure of one-dimensional TiO2 lepidocrocite

Hussein O. Badr, ^{1,5} Francisco Lagunas, ^{2,5} Daniel E. Autrey, ³ Jacob Cope, ¹ Takayuki Kono, ⁴ Takeshi Torita, A Robert F. Klie, Yong-Jie Hu, 1,* and Michel W. Barsoum 1,6,*

SUMMARY

We recently reported on the synthesis of one-dimensional (1D) TiO₂based nanofilaments, (NFs) by reacting water insoluble, earth abundant, and non-toxic Ti-containing precursors, such as TiC, TiB₂, and TiSi₂, among others, with quaternary ammonium hydroxides, mostly tetramethylammonium hydroxide at near-ambient conditions. From selected area diffraction, X-ray diffraction, and Raman spectroscopy, we previously concluded that the NF's structure was anatase-based. Herein, using high-resolution scanning transmission electron microscopy, Raman spectroscopy, obtained using low laser power, and density functional theory modeling, we conclude that the actual structure is 1D titania lepidocrocite-based structure with minimal cross sections of $\approx 5 \times 5 \text{ Å}^2$. The NFs grow along [100] with a and c lattice parameters of 3.78 \pm 0.01 Å and 3.04 \pm 0.06 Å. They tend to self-assemble/stack in two directions, viz. along the b and c axes. And while in-plane and out-of-plane interfilamentous distances are functions of the nature of the cations surrounding the NFs, the band gap, at \approx 4 eV, is not.

INTRODUCTION

Nanostructured (NS) titanium dioxides, TiO₂, have been, and remain, of significant research interest due to their unique physical and chemical properties, as well as their potential application in a wide range of fields including paint pigment, catalysis, photocatalysis, photoluminescence, gas sensors, and solar and fuel cells, among many others. 1-11 One dimensional (1D) and two-dimensional (2D) materials possess characteristics and properties that their three-dimensional (3D) counterparts do not. Arguably the most important difference is in their much higher surface areas. In terms of properties, low-dimensional solids allow for quantum confinement and more active catalytic sites.

Recently, we discovered a bottom-up, sol-gel based, one-pot, inexpensive, and highly scalable process to make TiO₂-based, 1D nanofilaments (NFs).¹² In our method, we simply immerse earth-abundant, non-toxic, water-insoluble binary or ternary titanium carbides, nitrides, borides, etc., in tetramethylammonium hydroxide (TMAH) aqueous solutions at temperatures in the 50°-85°C range for tens of hours under ambient pressures. This procedure converts the precursors to 1D NFs, which in turn self-assemble into quasi 2D flakes upon washing with water and filtering. 12

Based on a Raman spectroscopy anatase signature and selected area diffraction (SAD) in a transmission electron microscope (TEM) that agreed with our X-ray

PROGRESS AND POTENTIAL

Nanostructured titanium dioxides, TiO2, remain of significant research interest due to their potential use in a wide range of applications. Making such nanostructures is typically slow and/or hazardous, which renders their bulk production challenging and expensive. Recently, we discovered a one pot, nearambient method for producing one-dimensional (1D) TiO₂ nanofilaments (NFs) at the kilogram scale by reacting cheap and earth-abundant precursors, such as TiC, with common organic salts, e.g., tetramethylammonium hydroxide. In our first report, we concluded that the NF's structure was anatase. Herein, highresolution TEM, Raman, and XRD results show that the NF's structure is TiO₂ lepidocrocite instead. The NFs grow along the [100] direction, with the smallest cross sections of the order of $5 \times 5 \text{ Å}^2$, resulting in theoretical areas >1000 m²/g. The NFs selfassemble in- and out-of-plane. Deciphering the correct structure is a necessary first step to understanding and engineering properties.





diffraction (XRD) patterns and, more importantly, with bulk anatase, we concluded that the NFs were anatase-based.¹² We also concluded, based on the location of the arcs in the SAD patterns, that the NFs grow in the [200] and [110] directions of anatase.

More recent results, discussed herein, show that the NFs actually crystalize in a 1D lepidocrocite-based structure. The aim of this work is to present this new evidence, which includes new Raman spectra and fast Fourier transforms (FFT) of high-resolution scanning transmission electron microscope (STEM) micrographs. Based on the latter and starting with a density functional theory (DFT) generated structure we unambiguously show that the structure of our 1D NFs is lepidocrocite-based, henceforth referred to as one-dimensional lepidocrocite, or 1DL. We also show that the NFs only grow along the *a*, or the [100] direction, and stack along both *b* and *c* directions.

RESULTS AND DISCUSSION

Figure 1A plots XRD patterns (on a log scale) for 2 samples that were synthesized by reacting TiB_2 powders with TMAH at $80^{\circ}C$ for 5 days. After reaction, the resulting powders were washed with ethanol until the pH was ≈ 7 . In one case, the powders were dehydrated straight from ethanol at $50^{\circ}C$ in open air (bottom blue curve in Figure 1A). In the other case, sediments were further stirred in a LiCl solution, then rinsed with DI water before allowing the powders to, again, naturally dry in open air (top red curve in Figure 1A).

Vertical dashed lines in Figure 1A designate low-intensity unreacted TiB₂ peaks that were used as internal standards. When the powders were washed with ethanol, the XRD patterns were characterized by 7 basal reflections with a *d*-spacing of $\approx 11.5\,\text{Å}$, due to the stacking of 2D flakes comprising in-plane alignment of 1DL (see below). After washing with LiCl (see experimental procedures section), the *d*-spacing value dropped to $\approx 9.5\,\text{Å}$ confirming the replacement of TMA⁺ cations with Li⁺ ones. The yellow/green bands in Figure 1A denote lepidocrocite non-basal reflections, at 20 values of $\approx 26^{\circ}$, $\approx 48^{\circ}$, and $\approx 62^{\circ}$. These peak positions are in excellent agreement with our previous XRD patterns, as well as with rings previously observed in SAD patterns in TEM. 12

Figure 2A presents the Raman spectra of 7 samples processed in different ways outlined in Experimental procedures. In all cases, the spectra obtained were consistent with lepidocrocite. ¹³ In retrospect, it is now clear that the laser power used to obtain our previous spectra ¹² was too high, which resulted in a lepidocrocite-to-anatase transformation. This is best evidenced by the fact that when the laser power was increased, the Raman spectra changed from one consistent with lepidocrocite to one consistent with anatase (Figure 2B).

The next task is to reconcile the XRD patterns (Figure 1A) with the lepidocrocite structure. This is important here because, apart from the (200) peak at $\approx 48^{\circ}$ 20 and possibly the peak at $\approx 62^{\circ}$ 20, all other peaks are not standard lepidocrocite issue. 9,14 The latter is typically characterized by a strong (103) peak at $\approx 26-28^{\circ}$ 20, with a smaller (110) peak to its left. 9,14,15 Interestingly, Ma et al. published an XRD pattern for lepidocrocite nanotubes in which they assigned the peak at 62° 20 to (002). 15 Notably, their pattern included a large peak at 20 of $\approx 30^{\circ}$, which they assigned to (103). This is an important observation and suggests that the XRD signature of 1DL is the absence of that peak. To date, over 200 different samples were produced and in none did we see a (103) peak.

https://doi.org/10.1016/j.matt.2022.10.015

¹Department of Material Science and Engineering, Drexel University, Philadelphia, PA, USA

 $^{^2\}mathrm{Department}$ of Physics, University of Illinois at Chicago, Chicago, IL 60607, USA

³Department of Chemistry, Physics and Materials Science, Fayetteville State University, Fayetteville, NC 28301, USA

⁴Murata Manufacturing Co., Ltd, Nagaokakyo-shi, Kyoto, Japan

⁵These authors contributed equally

⁶Lead contact

^{*}Correspondence: yh593@drexel.edu (Y.-J.H.), barsoumw@drexel.edu (M.W.B.)





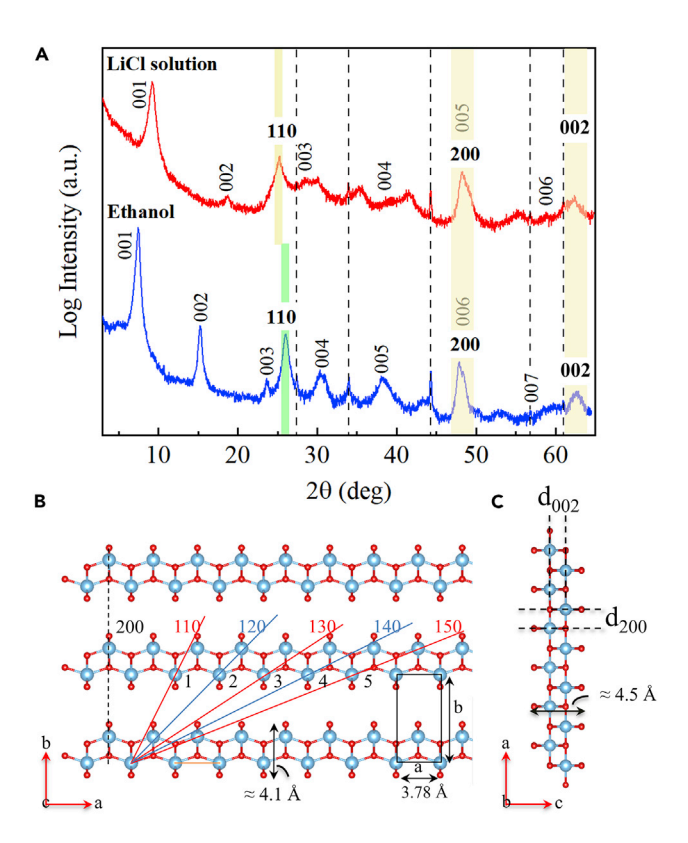


Figure 1. XRD patterns and DFT-generated 1DL structure

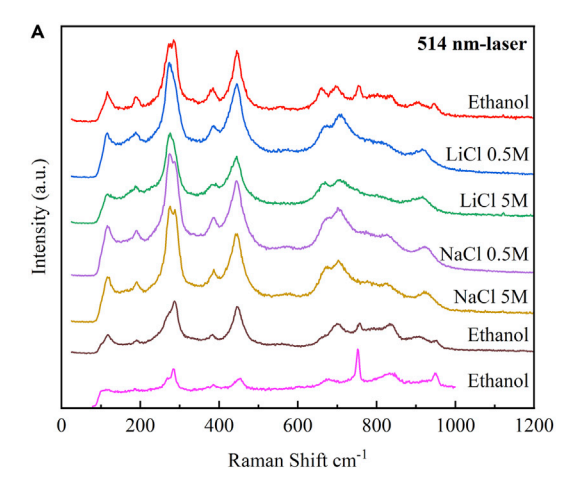
(A) XRD patterns of 2 samples: one washed with ethanol (bottom, blue), the other (red, top) washed with ethanol and then a 0.5 M LiCl solution (see Experimental procedures section). Positions of the (200) and (002) peaks at $2\theta \approx 48^\circ$ and $\approx 62^\circ$, respectively, are crystallographic and processing invariant; the positions of all other peaks are processing dependent. Note log scale on y axis. Yellow/green bands outline the 3 arcs/rings observed in SAD patterns of 2D flakes in TEM. Vertical dashed lines designate low-intensity unreacted TiB₂ peaks used as internal standards. ¹²

(B) Schematic of DFT-generated structure with TiO_2 ribbons stacked normal to b axis. Also traced by inclined red and blue are all non-basal planes predicted. Rectangle on bottom right denotes a unit cell with lattice parameters a and b. Note a is crystallographic but b depends weakly on spacing between ribbons, here chosen to be 7.5 Å. The same is true of stacking along 00L.

(C) Schematic of (001) plane assuming it is 2 Ti atoms wide. Spacing between 2 adjacent Ti atoms, along c, or d_{002} , is ≈ 1.5 Å, which gives rise to peak at $\approx 62^{\circ}$ 20 seen in XRD and SAD patterns. ¹² Also shown in (B) and (C) are the approximate thicknesses—measured from outermost O to outermost O—of 2-atom-thick Ti ribbons according to DFT calculations. Note that DFT results assume a 2D structure where the width of the ribbon in along c is infinite.

To illustrate the atomic structure of the observed self-assembled NFs, we made use of DFT calculations of a monolayer 2D lepidocrocite structure. Specifically, 2-Ti-atom-thick ribbons were cut from the DFT-relaxed 2D sheets and periodically stacked along the b direction (Figure 1B). Half the O atoms are 4-fold coordinated; the other half are 2-fold (excluding the O atoms at the ribbon edge). The unit cell corresponding to a perfect alignment of these NFs is shown by a black rectangular box in Figure 1B. The (200) peak in the XRD patterns is due to vertical plane labeled as such in Figure 1B. As discussed below, the planes responsible for the peak at 62° 2 θ are shown in Figure 1C and indexed as (002). In our coordinate system (Figure 1B), the peak at $\approx 26^{\circ}$ 2 θ is ascribed to the (110) planes (Figure 1B). Most of the other peaks are 00 ℓ peaks characteristic of 2D materials. Note that in the ethanol-washed samples (blue pattern in





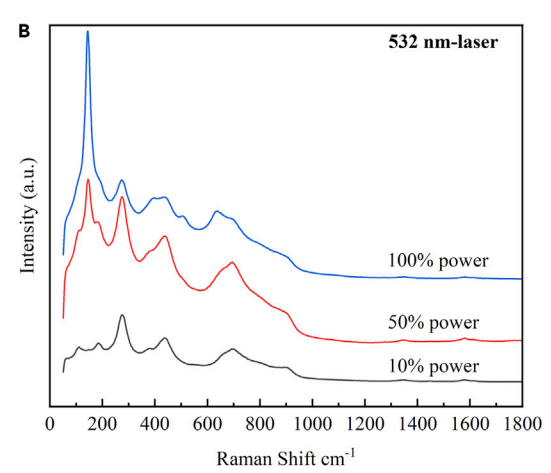


Figure 2. Raman spectra of 1 DL samples

(A) Samples were washed in media noted on panel (see Experimental procedures section). In all cases, the resulting spectra were consistent with those of lepidocrocite. All samples are shaker-processed except the two bottom ones, TiB_2 -derived (brown curve) and TiC-derived (magenta curve), which are magnetic stirrer-processed.

(B) Effect as a function of laser power. At high power, the material transforms from lepidocrocite (lower black spectrum) to anatase (top blue spectrum). The 10%, 50%, and 100% laser powers correspond to 6, 29, and 52 mWcm^{-2} , respectively.

Figure 1A), the order along the stacking direction is higher than in their LiCl-washed counterparts.

Figure 3 presents an annular bright field (ABF) STEM image of a TiB₂-derived bundle of NFs, together with an FFT of the center of the micrograph outlined by black dashed square. The high-angle annular dark field (HAADF) STEM image of this region shows crystalline contrast (see Figure S1).

To simulate the FFT, we again started with the same 2D DFT-generated lepidocrocite structure 16 and tilted it so the c axis was the zone axis. The lepidocrocite layers were stacked along the b axis (Figure 1B) such that the growth direction was [100] and, importantly, coincided with the bundle axis (middle lower inset in Figure 3). The stacking distance between the 2D layers was adjusted to match the (010) and (020) spots on the FFT (top right inset in Figure 3). The interlayer distance, henceforth referred to as d_{010} , chosen was 7.5 Å. The other spots (bottom right inset in Figure 3) were generated by the single-crystal diffraction module of the Crystal Maker software. Unless otherwise noted, only one adjustable parameter was used.

The agreement between the FFT spots and our simulated SAD—red circles in upper right inset in Figure 3—is excellent and suggests that the 110 and 200 d-spacings are 3.6 Å and 2.1 Å, respectively. The corresponding distances, derived from the XRD patterns for the (110) and (200) planes—henceforth referred to as d_{110} and d_{200} , respectively—were 3.5 \pm 0.8 Å and 1.89 \pm 0.01 Å.¹² Such a discrepancy in the d-spacings is not unexpected, especially when an FFT of an atomic-resolution STEM image is used. The position of the "diffraction spots" in the FFT is based on calibration of the underlying STEM image, which is affected by the accuracy of the underlying image calibration, scan distortions, and image pixel size. The fact that in the DFT calculations we model 2D lepidocrocite while experimentally we are dealing with 1DL could play a role. Also, the fact that our material may contain C,¹² but the DFT model does not, could prove important as we better understand where the C atoms reside. Needless to add, the XRD results are more accurate, but the





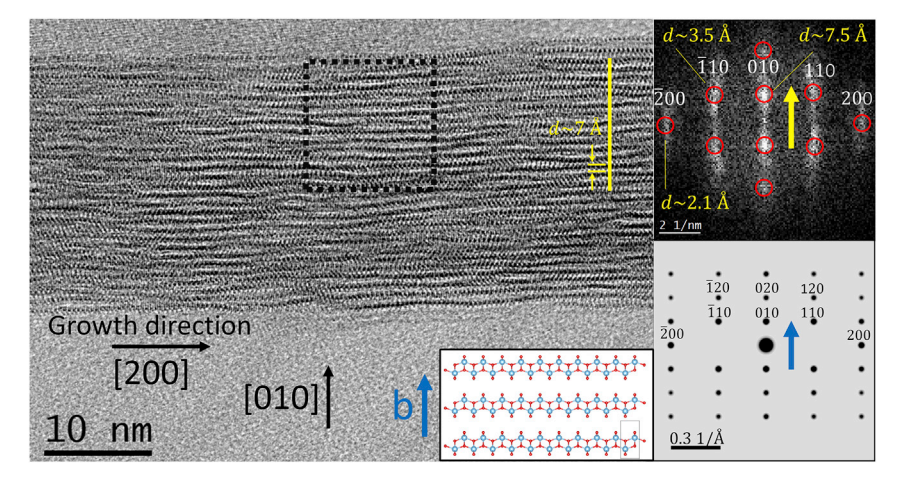


Figure 3. ABF STEM micrograph of a bundle of individual 1DL NFs oriented along the fiber axis Lower right inset is FFT of region outlined by black square. Lower middle inset shows schematic of lepidocrocite layers (not to scale) stacked along the b axis. Growth direction is along [200], which coincides with bundle axis. Superimposed on FFT (upper right inset), as red circles, are the indices predicted from the lepidocrocite DFT structure assuming spacing along b is 7.5 Å. Agreement between DFT-generated FFT and experiment is excellent. Planes (1,n,0) outlined in Figure 1B are denoted by blue and yellow arrows. Precursor was TiB₂, reacted in TMAH for 5 days at 80°C.

symmetry of the diffraction peaks is consistent. Based on the d_{200} value, the a lattice parameter is 3.78 Å, which is in slightly smaller than the 3.803 Å reported by Tominaka et al., ¹⁷ who also used TMAH to make 2D lepidocrocite.

In our previous work, we evidenced the 1D nature of our product by XRD, high-resolution TEM and SAD patterns, some of which were in the shape of arcs. 12 Coincidentally, the d-spacing obtained from the innermost arcs corresponded to an XRD peak $\approx 26^{\circ}$ 20, characteristic of anatase. This, together with the Raman results, convinced us that we were dealing with the anatase structure.

In the bright regions, where Ti-atomic columns presumably stack, it is possible to discern (as shown in Figures 4A and 4B) a zigzag pattern to the Ti-atoms that is consistent with schematic shown in Figure 1B.

Using the Scherer formula, we estimated the domain sizes along [110], [200], and [002] to be 4.2, 7.3, and 3.4 nm, respectively. These dimensions are small compared to the scale in the micrographs shown in Figures 3, 4, and 5, and suggest that the order is on a finer scale than the relatively larger features observed —viz. 2D flakes, fiber bundles, etc.

And while the crystalline regions were key for us to decipher the structure, it is also true that a good fraction of the bundles, or 2D flakes, were poorly crystallized. Figure 5 delineates two regions enclosed by a blue and a green square. The FFT pattern of the blue region (top inset in Figure 5) is clearly amorphous. The corresponding FFT (lower inset in Figure 5) of the green area resulted in a pattern that is the same as that shown in Figure 3, but significantly less sharp.

At this juncture it is important to critically assess our proposed structure. Based on DFT calculations, the thickness of the 2 Ti atom-thick ribbons, from outermost O to outermost O, is \approx 4.1 Å (Figure 1B). If the total interlayer distance is 7.5 Å, then the intergallery space is \approx 3.4 Å. This space is too small to accommodate a





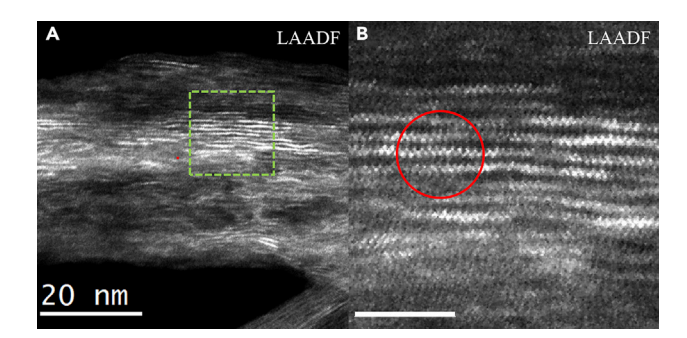


Figure 4. Low angle annular dark field STEM micrograph of sample shown in Figure 3

Sample shown at (A) low magnification and (B) higher magnification of region enclosed in green square in (A). Scale bar in 5 nm. Zigzag and 2-layered nature of Ti atoms in the NFs in area enclosed by red circle are clearly shown.

TMA cation. Consequently, the space must be filled with water and possibly surface terminations. Indirect evidence for this conclusion is that the change that occurs when the TMA $^+$ is replaced by Li $^+$ in the (00L) peaks is of the order of 2 Å, which is significantly larger than the changes in dimensions that occur to d₁₁₀ (Figure 1A).

Why the (0h0) peaks, which are clearly seen in the FFT (Figure 3), are missing from the XRD patterns is a mystery at this time. The origin of all other non-basal peaks can be traced to planes where the Ti atoms in one ribbon, or unit cell, are connected to an ever-increasing number of Ti atoms (numbered in Figure 1B) in adjacent ribbons as shown in Figure 1B. In our coordinate system, the first of these inclined planes is (110), with a d-spacing 3.5 that is consistent with an XRD peak at $\approx 26^{\circ}$ 20.

The *d*-spacing of the $\approx 62^\circ$ 20 peak does *not* match any of the (1,n,0) planes (Figure 1B) and does *not* appear in simulated FFT shown in top left inset in Figure 3. It thus must be associated with the *c* axis. The DFT c-lattice parameter (LP) is ≈ 3.01 Å and its (002) *d*-spacing, d_{002} , would be 1.5 Å, with a 20 of $\approx 62.2^\circ$. Experimentally in XRD patterns, this peak appears at 61.0 \pm 0.4°, ¹² corresponding to a *c*-LP of 3.04 \pm 0.06 Å. We thus ascribe this crystallographic peak to (002) reflections. As noted above, Ma et al. also reached the same conclusion. ¹⁵ Note that there are two (002) reflections; the first is associated with the stacking of the NFs along the *c* axis at 20 < 20° (Figure 1A); the second is crystallographic, and stems from the X-rays reflecting off the top of the ribbons shown in Figure 1C, and appears at $\approx 62^\circ$ 20. In Figure 1C, the ribbons' widths along the *c* axis—like those growing along the *a*-direction (Figure 1B)—are assumed to also be 2 Ti atoms thick. This is the minimum width possible and does not preclude wider ribbons.

In many of our SAD patterns of NFs self-assembled in various ways, but 3 rings were usually outlined. ¹² We erroneously associated them with the (101), (200), and (204) planes of anatase seen in the XRD patterns. ¹² These rings can now be ascribed to the (110), (200), and (002) planes of lepidocrocite. The *d*-spacings of these planes are in total agreement with their corresponding peaks highlighted yellow/green in Figure 1A.

Based on the aforementioned results, we identified 2 of the 3 planes of our 1DL NFs; (100) and (001). What about the third surface, (010)? In that surface, the Ti and O atoms are co-planar (Figure 1C). If that surface is cut such that only 2 Ti layers remain, they would also project a zigzag pattern (Figure 1C), that would be quite difficult to





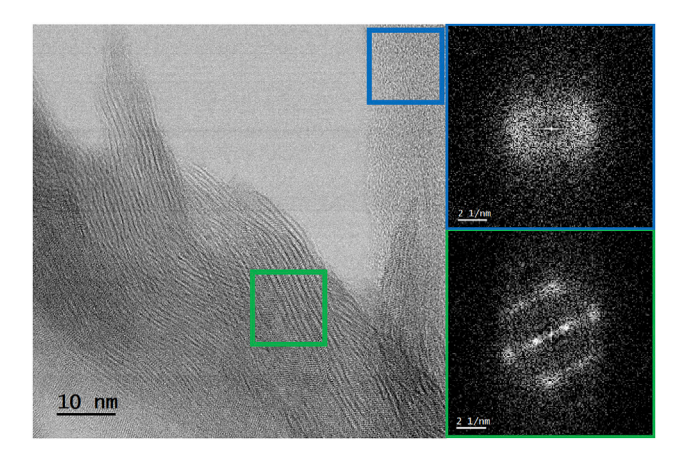


Figure 5. ABF STEM micrograph of same sample as in Figure 3, but focusing on different regions Top inset is FFT produced from blue square showing diffuse rings with no clear diffraction spots. Lower inset is FFT taken from green square showing clear diffraction spots indicating the region is largely crystalline.

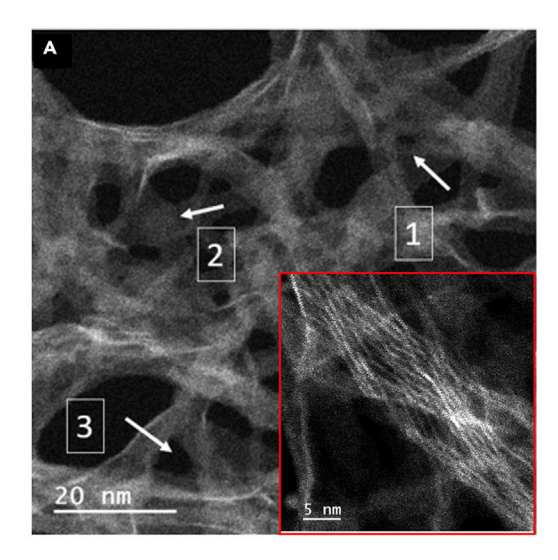
differentiate from the (001) surface that also results in a zigzag pattern (Figure 4). This comment notwithstanding, from the TEM image shown in Figure 3 and others, one can tentatively conclude that cross sections of the ribbons are in the 5 \times 5 \mathring{A}^2 range, which is a rounding off of their DFT widths of 4.1 (Figure 1B) and 4.5 Å (Figure 1C) and allows for possible surface terminations. Had this dimension been much wider, it is unlikely that the relatively homogeneous microstructure shown in Figure 3 would have been possible. As importantly, if relatively large crystalline segments existed, they would have been easily discernable in the TEM. These comments notwithstanding, we cannot at this time preclude the presence of wider segments along the c direction.

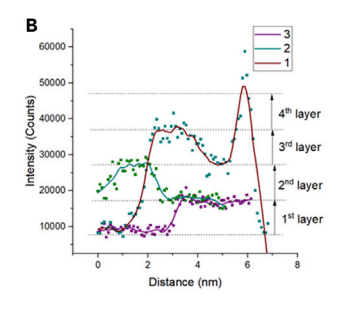
Along the same lines, it is well-established in MXene 18 and other 2D materials literature that it is non-trivial to find multilayers (ML) that are oriented "edge-on," since most of the 2D flakes lie with their basal planes parallel to the surface. ¹⁹ Typically, it is mostly at multilayer edges that flakes turn upwards, exposing their basal planes in an edge-on configuration. 18 Herein, the opposite is true; most regions are either poorly crystallized, amorphous, or exhibit an edge-on formation (Figures 3, 4, and 5). When 2D lepidocrocite, with strong (101) peaks in XRD, is imaged in a TEM, relatively large islands and lattice fringes are not difficult to find. 17,20 Their absence here strongly suggests they do not exist and what we have instead are 1DL NFs that self-assemble into 2D flakes. This is important because if the NFs seen herein are truly 1D, then we are dealing with NFs that are $\approx 5 \times 5 \text{ Å}^2$ in cross section. It is important in this context to emphasize that we are not implying that 2D layers do not exist; the XRD patterns are clear. In other words, we are saying that the 2D flakes are composed of 1DL NFs that self-assemble into layers.

Figure 6 shows a HAADF STEM image of a loose bundle of NFs that bolsters the conclusion that we are dealing with NFs at least in some of the areas that appear amorphous. In this TiC-derived sample, individual NFs can be readily discerned (inset in Figure 6A).

While regions that aligned themselves along the [100] direction showed clear signs of crystalline contrast (Figure 3), the sample contained many regions where no atomic contrast could be observed. In a TiC-derived sample—prepared on TEM







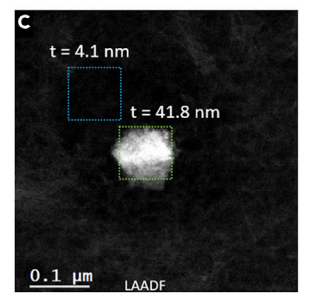


Figure 6. STEM characterization of TiC-derived NFs, as well as unreacted particles

(A) HAADF image of a loose bundle of NFs. Inset shows higher magnification image. Regions of reduced intensity without visible atomic contrast are likely NFs not oriented along a low zone axis. (B) Integrated line scans show the intensity of these regions scale as integer multiples of intensity measured in line scans denoted in (A) by respective numbers.

(C) LAADF image of an unreacted TiC particle surrounded by a web-like structure composed of NFs; thickness estimates based on EELS spectra maps are shown to be 4.1 nm for web-like structure and 41.8 nm for unreacted TiC particle. Precursor was TiC, reacted in TMAH for 5 days at 80°C.

grids with no carbon support—the lack of crystalline contrast (Figure 6A) most probably arises from misoriented NFs instead of amorphous material. Considering the larger cross sectional area, we suspect that these NF are aligned along [001] and increased contrast arises from quanta (1, 2, 3, etc.) of stacked NFs. To support this conclusion, we integrated regions from the HAADF image shown in Figure 6A. Since the contrast from the HAADF images arises from mass thickness, the intensity measured from the integrated line scans correlate with specimen thickness in that region. White arrows in the HAADF image (Figure 6A) point to three regions where line scans were collected and plotted in Figure 6B. Despite a low signal to noise ratio, there are visible plateaus in the scan profiles. To better visualize these plateaus, we smoothed the profiles using a Savitzky-Golay method with the points of window set to 15. These smooth profiles are shown as lines in Figure 6B, while the raw data is overlaid as a scatterplot. Taking the thinnest region as a single layer, we see the other plateaus fall within integer multiples of this value.

And while these line scans provide a relative measure of thickness, we used EELS spectra to estimate the absolute thickness of various regions. The LAADF image (Figure 6C) shows a region with an unreacted TiC particle at its center, surrounded





by a web of NFs. In this same region, we collected simultaneous core and low loss spectra maps, shown in Figures S2A and S2B, respectively. From measurements of the intensity of the zero-loss peak in the low-loss spectra and an estimate of the effective atomic number from the elemental compositions calculated from core loss spectra, we estimated the thicknesses at different regions of the EELS maps. The calculated thickness in the NF web area—outlined with dashed blue box—was 4.1 nm. Coincidentally or not, this value is close to the 3.4 nm average domain size along [001] calculated by the Scherrer formula. To test the validity of this value, we measured the absolute thickness in the region of the unreacted TiC particle (Figure S2A). Considering the particle is roughly 50 nm in diameter and cubic, the estimated thickness of \approx 42 nm appears a reasonable estimate. These estimates were conducted using the built "Elemental Quantification" in GMS 6.50.2584.00. (For details of the elemental compositions and models for thickness estimates, refer to Supplemental information.).

It is important at this juncture to validate the conclusions reached above. Of the 3 distances, d_{200} , d_{002} , and d_{110} , only the first 2 are *crystallographic*. It is for this reason that for all materials produced to date—over 200 separate runs—the locations of the 200 peaks, at $\approx 48^{\circ}$ 20, never changed (Figure 1A). The same is true of the $\approx 62^{\circ}$ 20 peaks. The locations of the (110) peaks, on the other hand, are a function of the surrounding cations (Figure 1A) and thus cannot be crystallographic. Another important observation consistent with this notion is that the distance between NFs along the yellow line plotted in Figure 3 is ≈ 7 Å, which is comparable to the 7.5 Å used to adjust theory to the FFT patterns.

Compared to 2D materials with 1 stacking direction, here there are two; one along the (010) direction or b axis (lower left inset in Figure 3); the other is out-of-the plane of the page (along the c axis) that is responsible for the low angle reflections labeled (00 ℓ) in Figure 1. Not much information can be gleaned from the STEM images about the c axis spacing or stacking. Not surprisingly, that spacing is also a function of the nature of the cations surrounding the NFs as shown by peaks labeled (00 ℓ) in Figure 1. Note, most of the peaks, and the strongest ones, are (00 ℓ) peaks. This is especially manifest when the γ axis is plotted linearly and not logarithmically.

Lastly, while the washing protocol changes the spacing between NFs, these variations do not affect the band gap. Tauc plots (Figure 7) confirm the presence of as indirect band gap at ≈ 4 eV. Averaging 10 different runs reported on earlier 12 and those measured herein, the average band gap is found to be 4.0 \pm 0.1 eV. We note in passing and as discussed in our previous work, 12 this band gap energy is a record for a TiO $_2$ -based material made via a bottom-up approach and is an independent confirmation of a quantum confinement effect. There are numerous reports in the literature on 1D TiO $_2$ -based materials. As far as we are aware, however, none of them report a quantum size effect on the band gap.

Before concluding it is worthwhile to review the energies of different 2D titania-based structures. Table 1 summarizes our and others' DFT results. At 0 K, DFT calculations show that *bulk* anatase is more stable than 2D sheets of TiO_2 lepidocrocite. We calculate an energy difference (ΔH_{rel}) between the two structures to be 0.055 eV/atom (last row in Table 1). A value of 0.052 eV/atom is reported in the literature. Furthermore, the 2D lepidocrocite structure is *more* stable than all other common 2D TiO_2 polymorphs, including the (101) anatase cuts of various thicknesses as shown in Table 1. The structures with 2 O replaced by one C can be found in our previous work. Here we are modeling pure 2D TiO_2 lepidocrocite. This is a



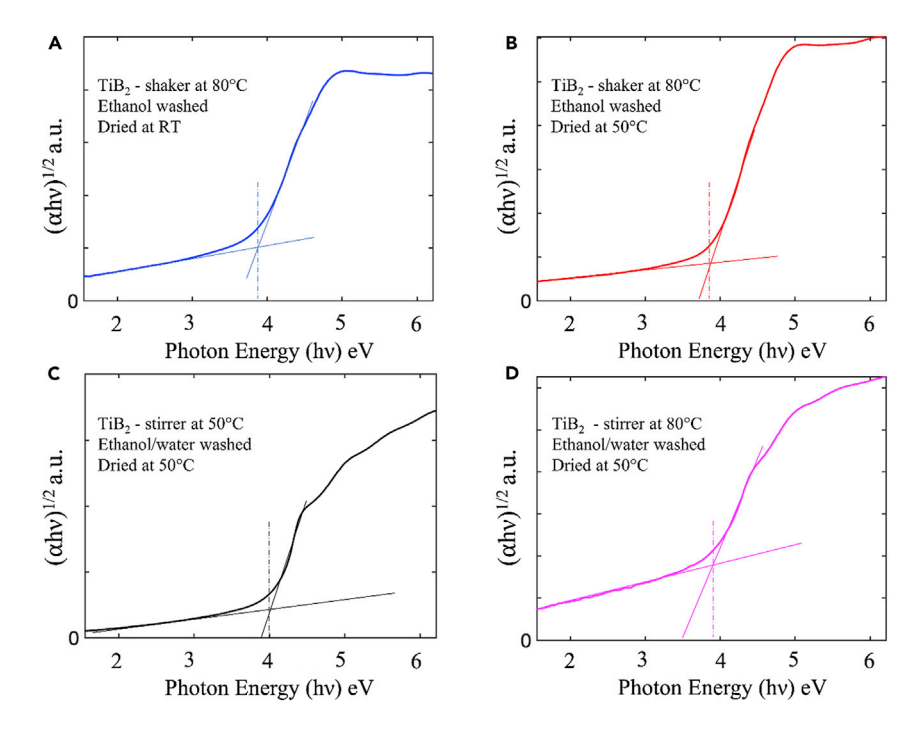


Figure 7. Tauc plots as a function of various synthesis and washing procedures shown on each panel

Also see the Experimental procedures section.

crucial result and explains why the polymorph we observe is lepidocrocite-based and not 2D anatase. Note the DFT calculations assume 2D sheets rather than 1D NFs. We are currently working on modeling 1DL NFs.

Conclusions

In conclusion, the 1D NFs produced by reacting TiB_2 and TiC powders in TMAH at $80^{\circ}C$ for 5 days crystalize in a lepidocrocite TiO_2 structure. The NFs grow in the [100] direction and stack along the b-direction in the plane that the NFs self-assemble to either create bundles (Figure 3) or larger 2D flakes shown in our previous work. ¹² And while the crystalline regions are key for us to understand the structure, it is also true that a good fraction of the bundles, or 2D flakes, are poorly crystallized. Some areas appear amorphous.

Regardless of how well the NFs are self-assembled, their theoretical specific surface area, assuming a density of 4.25 g cm³ and a minimal thickness of 0.45 nm, is of the order of $\approx 1,000~\text{m}^2/\text{g}$. This is an extraordinary number for a Ti-containing material and partially explains some of the remarkable properties these materials exhibit. The fact that the process to make them is inexpensive, highly scalable—we routinely make 100 g batches in a laboratory setting—and the precursors powders, such as TiC, TiB2, Ti-containing MAX phases, are earth abundant, and non-toxic bodes well for their large-scale application in myriad fields.

EXPERIMENTAL PROCEDURES

Resource availability

Lead contact

Further information and requests for resources and reagents should be directed to and will be fulfilled by the lead contact, Michel W. Barsoum (barsoumw@drexel.edu).





Table 1. Summary of experimental and DFT results for bulk anatase, 2D anatase, and lepidocrocite $^{11,21-23}$

Structure		a ₀ (Å)	b ₀ (Å)	c ₀ (Å)	ΔH_{ref} (eV/atom)
Bulk anatase	Experiment	3.782 ²²		9.502 ²²	0
	Theory-ref	3.78 ¹¹ 3.80 ²¹		9.64 ¹¹ 9.70 ²¹	
	This work	3.805		9.729	
(101)-2D anatase ^a	Experiment	3.76ª	10.45ª		
2-layer Ti	This work	3.538	10.476		0.140
4-layer Ti		3.732	10.447		0.079
6-layer Ti		3.750	10.429		0.059
Lepidocrocite	This work and Orzali et al. ²³	3.78 (exp) 3.72 ²³		3.02 ²³	
	Theory-ref	3.75 ²¹ 3.75 ¹¹		3.02 ²¹ 3.01 ¹¹	0.052 ²¹ 0.05 ¹¹
	This work	3.75		3.03	0.055

^aSee our previous work.¹²

Last column lists energy difference between various 2D titania structures and bulk anatase.

Materials availability

All structural data and information generated in this study are available from the lead contact.

Data and code availability

This study did not generate datasets and code.

Materials synthesis and processing

Samples of 1DL NFs prepared by shaking TiB_2 (Thermo Scientific, -325) powders with tetramethyl ammonium hydroxide aqueous solution, TMAH (Alfa Aesar, 25 wt % in DI water, 99.9999%) at 80°C for 5 days using a temperature-controlled shaking incubator (Labnet 211DS, 49L, 120V, NJ). In all cases, the Ti:TMAH mole ratio was kept at 0.6. After reaction, the resulting powders were washed with ethanol (Decon Lab Inc., 200 proof) until pH was ≈ 7 . The powders were then dehydrated in open air at 50°C overnight. To explore any potential effect of the drying temperature, another sample, from the same batch, was dehydrated at room temperature, RT, instead.

To assess the capability of ion exchange, ethanol-washed sediments were further stirred, while wet, 3 subsequent times each of 6 h in one of the following salt solutions: LiCl 0.5M, LiCl 5M, NaCl 0.5M, or NaCl 5M and then rinsed with DI water 3 times to remove any unreacted salt or reaction products. All salts were purchased from Alfa Aesar with >99% purity. The LiCl- and NaCl-washed powders were then air-dried at 50°C, similar to above.

To compare shaker-processed samples to those produced using magnetic stirring, 12 in some cases TiB $_2$ or TiC powders were magnetically stirred, at 300 rpm, in a TMAH solution following the above-mentioned conditions of mole ratio, temperature, and time. After reaction, the resulting slurry was washed 6 times with ethanol until pH was ≈ 7 , redispersed in DI water, shook for 5 min, then centrifuged at 3,500 rpm for 30 min. The resulting colloidal suspension was then filtered using vacuum-assisted filtration to produce a filtered film that was dried at 50°C in open air overnight.

The Raman spectra shown in Figure 2 were obtained for the following seven samples: ethanol washed, LiCl 0.5M, LiCl 5M, NaCl 0.5M, NaCl 5M solutions and the magnetically stirred TiB₂- and TiC-derived samples.



X-ray diffraction, XRD

XRD patterns were acquired using a diffractometer (Rigaku MiniFlex) operated with Cu K_{α} radiation (40 kV and 15 mA) in the 2–65° 20 range with step size of 0.02° and a dwell time of 1 s. All XRD patterns were obtained from powders dried overnight at 50°C in open air.

Raman spectroscopy

Two sets of Raman spectra were obtained in two different labs. At Drexel University, Raman spectra were collected at room temperature in air. Measurements were done with an inverted reflection mode Renishaw InVia (Gloucestershire, U.K.) instrument equipped with $63 \times (NA = 0.7)$ objectives and a diffraction-based room temperature CCD spectrometer. An Ar⁺ laser (514 nm) was used, and the laser power was kept in the \sim 0.1–0.5 mW range.

In another set, obtained at Fayetteville State University, suspensions of TiB2-derived material with a concentration of 10 mg/mL were prepared with ethanol (>99.7%, Sigma Aldrich, St. Louis, MO) and were drop-cast onto a microscope slide and allowed to air dry at RT, for 24 h. Raman spectra were collected at RT using an XploRA PLUS confocal Raman microscope (Horiba Scientific, Piscataway, NJ, USA) with a 250 mm focal length spectrometer in a backscatter geometric configuration. The spectrometer was first calibrated using a silicon chip with excitation by an air-cooled 532 nm solid state laser (100 mW) and using a 100x (NA = 0.9 and WD = 0.21 mm) objective to obtain a 1 μ m spot size. A 1200 gr/mm grating was used, and the scattered light was collected with a thermoelectrically (TE) air-cooled charge-coupled device (CCD) detector with 1024x256 pixels for a spectral resolution of 1 cm⁻¹. A neutral density (ND) filter wheel was used to attenuate the laser power to 10%, 25%, 50%, or 100%, and spectra were acquired at a lower power (10%) or higher. Raman spectra were collected in the 75-1200 cm⁻¹ range with 2 s integration time and 64 accumulations. The LabSpec 6 software was used to fit the collected Raman spectrum according to the Gaussian-Lorentzian function to obtain the peak positions and their intensities.

Transmission electron microscopy

Atomic scale characterization was conducted using an aberration-corrected, cold-field emission TEM (JEOL ARM200CF) operated at a 200kV primary electron energy. Imaging was conducted with the emission current at 15 μA and an electron probe semi-convergence angle of 24 mrad, resulting in an electron probe size of approximately 80 pm. Annular bright field (ABF) imaging, which is a coherent imaging technique, was conducted using an outer angle of 23 mrad and an inner angle of 11 mrad. For low angle annular dark field (LAADF) imaging the inner and outer angles were 30 and 120 mrad, respectively. HAADF images were collected with 68 and 280 mrad inner and outer detector angles, respectively. The primary contrast mechanism for HAADF imaging is related to the square of the average atomic number and the total thickness of the atomic columns.

The TEM samples were prepared by dispersing nanofilament powders in 5 mL of methanol. The solution was drop cast onto a 3 mm copper mesh coated with a lacey carbon film and allowed to dry for an hour. The TEM grid was then loaded onto a plasma cleaned double tilt holder and inserted into the microscope column.

Electron energy-loss spectroscopy (EELS)

EELS measurements were conducted using a post-columns Gatan Continuum GIF ER spectrometer, with an electron probe semi-convergence angle of 17.8 mrad and a collection angle of 53.4 mrad.





Density functional theory calculations

First-principles calculations were carried out to study the atomic structures and ground state energies of bulk anatase and several polymorphic structures of 2D TiO2. The calculations were performed using the projector-augmented wave (PAW) method as implemented in the Vienna Ab initio Simulation Package (VASP).^{29,30} The exchange-correlation functional was depicted by the general gradient approximation from Perdew, Burke, and Ernzerhof (GGA-PBE).³¹ The cutoff energy of the plane wave basis is set to be 600 eV. Brillouin zone integration was performed using the Gaussian smearing method, with a smearing width of 0.10 eV, and an automatic k-point meshing scheme implanted in VASP with a Rk length of 45 $\mbox{\normalfont\AA}$. The convergence criterion of the electronic self-consistent loop was set as 10^{-6} eV. The input supercells were fully relaxed until the Hellmann-Feynman forces on each atom were smaller than 5 meV/Å.

The calculations for the 2D-TiO₂ were all performed for a monolayer sheet by introducing a 15 Å vacuum region along the normal direction of the sheet surface to eliminate the interactions between the 2D sheets with their periodic images.

To generate the atomic structure illustrations in Figures 1B and 1C, a 1D ribbon structure with a thickness of two Ti-O polyhedral was cut from the relaxed structure of the 2D lepidocrocite along the [100] direction. Then, the ribbon structure is periodically stacked along the [010] direction with a chosen separation distance of 7.5 Å. Note that first-principles relaxation calculations were not performed for the 1D ribbon structure.

SUPPLEMENTAL INFORMATION

Supplemental information can be found online at https://doi.org/10.1016/j.matt. 2022.10.015.

ACKNOWLEDGMENTS

This work was funded by Ceramics Program of Division of Materials Research of the National Science Foundation (NSF) (grant no. 2211319) and Murata Manufacturing of Japan. D.E.A. would like to acknowledge financial support of NSF HBCU-UP RIA (HRD 1800795) and Tamara N. Hewett, a grant-supported undergraduate for acquisition of Raman spectra. R.F.K. acknowledges support from the NSF(DMR-1831406). The acquisition and upgrade of the UIC JEOL JEM ARM200CF was supported by an MRI-R² grant (DMR-0959470) and an MRI-grant (DMR-1626065) from NSF.

AUTHOR CONTRIBUTIONS

H.O.B. and M.W.B. conceived the idea and supervised all experimental work. F.L. and R.F.K. conducted TEM and EELS experiments and analysis. D.E.A. and T.K. carried out Raman work and analysis. J.C. synthesized samples in the lab. T.T. helped in data analysis and discussions. Y.-J.H. conducted all DFT work and measurements. M.W.B. also supervised the project and wrote the manuscript. All authors discussed the results and commented on the manuscript.

DECLARATION OF INTERESTS

A provisional patent application entitled "Bottom-Up, Scalable Synthesis of Oxide-Based Sub-Nano And Nanofilaments And Nanofilament-Based Two-Dimensional Flakes and Mesoporous Powders" naming Michel W. Barsoum and Hussein



O. Badr was filed on August 17, 2022. The remaining authors declare no competing financial interests.

Received: August 25, 2022 Revised: September 18, 2022 Accepted: October 19, 2022 Published: November 2, 2022

REFERENCES

- 1. Kumar, S.G., and Devi, L.G. (2011). Review on modified TiO₂ photocatalysis under UV/visible light: selected results and related mechanisms on interfacial charge carrier transfer dynamics. J. Phys. Chem. A 115, 13211-13241. https://doi. org/10.1021/jp204364a.
- 2. Schaub, R., Thostrup, P., Lopez, N., Lægsgaard, E., Stensgaard, I., Nørskov, J.K., and Besenbacher, F. (2001). Oxygen vacancies as active sites for water dissociation on rutile TiO₂ (110). PRL 87, 266104.
- 3. Wang, A.S.D., and Sasaki, T. (2014). Titanium oxide nanosheets: graphene analogues with versatile functionalities. Chem. Rev. 114, 9455-9486.
- 4. Bourikas, K., Kordulis, C., and Lycourghiotis, A. (2014). Titanium dioxide (anatase and rutile): surface chemistry, liquid-solid Interface chemistry, and scientific synthesis of supported catalysts. Chem. Rev. 114, 9754-9823. https:// doi.org/10.1021/cr300230q.
- 5. Wang, X., Li, Z., Shi, J., and Yu, Y. (2014). Onedimensional titanium dioxide nanomaterials: nanowires, nanorods, and nanobelts. Chem. Rev. 114, 9346-9384.
- 6. Ramos-Delgado, N.A., Gracia-Pinilla, M.Á., Mangalaraja, R.V., OʻShea, K., and Dionysiou, D.D. (2016). Industrial synthesis and characterization of nanophotocatalysts materials: titania. Nanotechnol. Rev. 5, 467-479. https://doi.org/10.1515/ntrev-2016-0007.
- 7. Fang, W., Xing, M., and Zhang, J. (2017). Modifications on reduced titanium dioxide photocatalysts: a review. J. Photochem. Photobiolog C: Photochem. Rev. 32, 21–39.
- 8. Saeed, M., Muneer, M., and Akram, N. (2021). Photocatalysis: an effective tool for photodegradation of dyes—a review. Environ. Sci. Pollut. Res. 1–19.
- 9. Sasaki, T., Watanabe, M., Michiue, Y., Komatsu, Y., Izumi, F., and Takenouchi, S. (1995). Preparation and acid—base properties of a protonated titanate with the lepidocrocite-like layer. Chem. Mater. 7, 1001.
- 10. Sasaki, T., and Watanabe, M. (1997). Semiconductor nanosheet crystallites of quasi-TiO₂ and their optical properties. J. Phys. Chem. B 101, 10159-10161.
- 11. Zhou, W., Umezawa, N., Ma, R., Sakai, N., Ebina, Y., Sano, K., Liu, M., Ishida, Y., Aida, T., and Sasaki, T. (2018). Spontaneous direct band gap, high hole mobility, and huge exciton energy in atomic-thin TiO₂ nanosheet. Chem.

- Mater. 30, 6449-6457. https://doi.org/10.1021/ acs.chemmater.8b02792.
- 12. Badr, H.O., El-Melegy, T., Carey, M., Natu, V., Hassig, M.Q., Johnson, C., et al. (2022). Bottom-up, scalable synthesis of anatase nanofilament-based two-dimensional titanium carbo-oxide flakes. Mater. Today 54, 8-17. https://doi.org/10.1016/j.mattod.2021.10.033.
- 13. Hu, W., Li, L., Li, G., Liu, Y., and Withers, R.L (2014). Atomic-scale control of TiO₆ octahedra through solution chemistry towards giant dielectric response. Sci. Rep. 4, 1-9. https:// doi.org/10.1038/srep06582
- 14. Esmat, M., Farghali, A.A., El-Dek, S.I., Khedr, M.H., Yamauchi, Y., Bando, Y., et al. (2019). Conversion of a 2D lepidocrocite-type layered titanate into its 1D nanowire form with enhancement of cation exchange and photocatalytic performance. Inorg. Chem. 58, 7989-7996. https://doi.org/10.1021/acs. inorgchem.9b00722.
- 15. Ma, R., Bando, Y., and Sasaki, T. (2003). Nanotubes of lepidocrocite titanates. Chem. Phys. Lett. 380, 577–582. https://doi.org/10. 1016/j.cplett.2003.09.069.
- 16. Reeves, K.G., Ma, J., Fukunishi, M., Salanne, M., Komaba, S., and Dambournet, D. (2018). Insights into Li⁺, Na⁺, and K⁺ Intercalation in lepidocrocite-type layered TiO₂ structures. ACS Appl. Energy Mater. 1, 2078-2086. https:// doi.org/10.1021/acsaem.8b00170
- 17. Tominaka, S., Yamada, H., Hiroi, S., Kawaguchi, S.I., and Ohara, K. (2018). Lepidocrocite-type titanate formation from isostructural prestructures under hydrothermal reactions: observation by synchrotron X-ray total scattering analyses. ACS Omega 3, 8874-8881. https://doi.org/10.1021/acsomega.8b01693.
- 18. Naguib, M., Kurtoglu, M., Presser, V., Lu, J., Niu, J., Heon, M., Hultman, L., Gogotsi, Y., and Barsoum, M.W. (2011). Two dimensional nanocrystals produced by exfoliation of Ti₃AlC₂. Advan. Mater. 23, 4248–4253.
- Coleman, J.N., Lotya, M., O'Neill, A., Bergin, S.D., King, P.J., Khan, U., Young, K., Gaucher, A., De, S., Smith, R.J., et al. (2011). Twodimensional nanosheets produced by liquid exfoliation of layered materials. Science 331, 568.
- 20. Ma, J., Reeves, K.G., Porras Gutierrez, A.-G. Body, M., Legein, C., Kakinuma, K., et al. (2017) Layered lepidocrocite type structure Isolated by revisiting the sol-gel chemistry of anatase

- TiO₂: a new anode material for batteries. Chem. Mater. 29, 8313-8324.
- 21. Eivari, H.A., Ghasemi, S.A., Tahmasbi, H., Rostami, S., Faraji, S., Rasoulkhani, R., Goedecker, S., and Amsler, M. (2017). Twodimensional hexagonal sheet of TiO2. Chem. Mater. 29, 8594-8603.
- 22. Burdett, J.K., Hughbanks, T., Miller, G.J. Richardson, J.W., Jr., and Smith, J.V. (1987). Structural-electronic relationships in inorganic solids: powder neutron diffraction studies of the rutile and anatase polymorphs of titanium dioxide at 15 and 295 K. J. Am. Chem. Soc. 109, 3639-3646.
- 23. Orzali, T., Casarin, M., Granozzi, G., Sambi, M., and Vittadini, A. (2006). Bottom-up assembly of single-domain titania nanosheets on (1×2)— Pt (110). Phys. Rev. Lett. 97, 156101.
- 24. Klie, R.F., Gulec, A., Guo, Z., Paulauskas, T., Qiao, Q., Tao, R., Wang, C., Low, K.B., Nicholls, A.W., and Phillips, P.J. (2014). The new JEOL JEM-ARM200CF at the University of Illinois at Chicago. Cryst. Res. Tech. 49, 653-662. https:// doi.org/10.1002/crat.201300200.
- 25. Phillips, P.J., and Klie, R.F. (2013). On the visibility of very thin specimens in annular bright field scanning transmission electron microscopy. Appl. Phys. Lett. 103, 033119. https://doi.org/10.1063/1.4816081.
- 26. Findlay, S.D., Shibata, N., Sawada, H., Okunishi, E., Kondo, Y., Yamamoto, T., and Ikuhara, Y. (2009). Robust atomic resolution imaging of light elements using scanning transmission electron microscopy. Appl. Phys. Lett. 95, 191913.
- 27. Pennycook, S.J., and Boatner, L.A. (1988). Chemically sensitive structure-imaging with a scanning-transmission electron-microscope. Nature 336, 565–567.
- 28. Nellist, P.D., and Pennycook, S.J. (1999). Incoherent imaging using dynamically scattered coherent electrons. Ultramicroscopy *78*, 111–124.
- 29. Bloechl, P.E. (1994). Projector augmentedwave method. Phys. Rev. B 50, 17953.
- 30. Kresse, G., and Furthmüller, J. (1996). Efficient iterative schemes for ab initio total-energy calculations using a plane-wave basis set. Phys. Rev. B 54, 11169-11186.
- 31. Perdew, J.P., Burke, K., and Ernzerhof, M. (1996). Generalized gradient approximation made Simple. Phys. Rev. Lett. 77, 3865-3868.